OpenFOAM® Journal

Volume 6 [Review Papers], Pages 60–78
ISSN: 2753-8168

Steady RANS Modeling of the Atmospheric Boundary Layer: A Systematic Review and Some Practical Guidelines

Ivan Batistić[1,*], Mihael Cindori[2], Severino Krizmanić[1], Ivo Džijan[1], Franjo Juretić[3], Petar Škvorc[1,4], and Hrvoje Kozmar[1]

Email address: ivan.batistic@fsb.unizg.hr, mihael.cindori@gmail.com, severino.krizmanic@fsb.unizg.hr, ivo.dzijan@fsb.unizg.hr, franjo.juretic@cfmesh.com, pskvorc@foi.unizg.hr, hrvoje.kozmar.fsb.unizg.hr

[1] Faculty of Mechanical Engineering and Naval Architecture, University of Zagreb, Ivana Lučića 5, 10000 Zagreb, Croatia

[2] Ecodica d.o.o., Gorjanska ulica 23, 10000 Zagreb, Croatia

[3] Creative Fields d.o.o., Avenija Dubrovnik 15, 10000 Zagreb, Croatia

[4] Faculty of Organization and Informatics, University of Zagreb, Pavlinska 2, 42000 Varaždin, Croatia

DOI: https://doi.org/10.51560/ofj.v6.166
Results with version(s): OpenFOAM® v2406
Repository: https://github.com/iBatistic/RANS-ABL-OpenFOAM

Abstract. Accurate modeling of the neutrally stratified atmospheric boundary layer (ABL) is essential for computational wind engineering applications. The present study provides a comprehensive review of the ABL modeling approaches performed using Reynolds-averaged Navier-Stokes (RANS) equations. The main focus is on the different mechanisms used to drive the ABL flow and the corresponding boundary-condition formulations. Three major ABL modeling approaches were assessed, i.e., shear stress-driven, pressure-driven, and body force-driven flows, in terms of theoretical formulation, code implementation, and practical applications. The study addresses the role of the near-wall modeling, particularly the effects of wall functions that account for surface roughness using the aerodynamic surface roughness length and Nikuradse roughness parameter. A comparative analysis of these models is presented based on their ability to account for turbulence characteristics while maintaining the flow homogeneity. Computational simulations performed in OpenFOAM were used to assess the computational setup in these three approaches. This work generally serves as a guideline for selecting the most suitable ABL model for specific CFD applications, including urban wind studies, pollutant dispersion, and structural aerodynamics.

1. Introduction

Accurate turbulence modeling in computational simulations of the atmospheric boundary layer (ABL) is crucial for properly studying wind effects on structures. While Large Eddy Simulation (LES) [1–4] has gained interest in recent years, Reynolds-averaged Navier-Stokes (RANS) models are still preferred due to their simplicity and little demand regarding computational resources.

Previous work on the computational modeling of the ABL using the finite volume method (FVM) and RANS turbulence models exhibited the significance of the horizontal flow homogeneity with particular emphasis on the: a) inlet profiles and boundary conditions [5,6], b) near-wall flow modeling [5,7], and c) inactive turbulence [8,9]. It has been proven that the flow homogeneity along computational domain is essential to avoid discrepancies between the computational and experimental data [10]. Flow homogeneity implies that mean flow and turbulence quantities vary only with height and remain constant in the streamwise direction. In this case, the characteristic flow profiles at the inlet of the computational domain do not alter along the domain, i.e., the profiles at the location of the studied engineering structures (incident profiles) remain identical to the inlet profiles, see Fig. 1.

* Corresponding author

Received: 21 May 2025, Accepted: 13 February 2026, Published: 11 March 2026

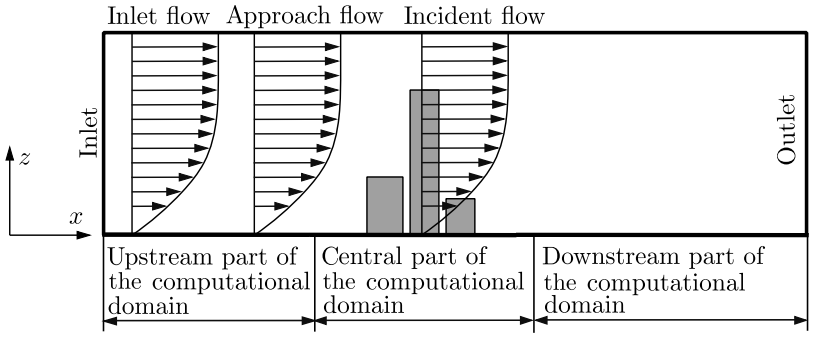

Figure 1. Computational domain with embedded building models for the CFD simulation of the ABL flow, adapted from [7].

For the flow modeling in the immediate vicinity of a solid wall, previous studies relied on the application of wall functions that account for surface roughness. In such approaches, the viscous sublayer ($y^+ \lesssim 5$) is not explicitly resolved; it is modelled using the wall functions evaluating the value of values of flow variables at the cell centres [11]. Two types of wall functions have been commonly employed, i.e., a) wall functions based on Nikuradse roughness height [7,12], b) wall functions based on the aerodynamic surface roughness length [5]. Wall functions based on Nikuradse roughness are included in most computational packages. The Nikuradse roughness height is not proportional to the aerodynamic surface roughness length, which is a key parameter for describing the ABL flow. It is therefore necessary to establish the link between the surface roughness length and the equivalent Nikuradse roughness height [7].

The effect of inactive turbulence is commonly modeled by modifying the constants of the employed RANS turbulence model [13–15], which may yield inaccurate results for the flow around buildings [15, 16] and flow over hilly terrain [17, 18]. Previous studies have shown that modifying turbulence-model constants can significantly influence momentum transport and TKE in the ABL due to the presence of inactive turbulence [19–21]. This concept is based on Townsend's hypothesis [8, 9], which indicates that turbulence near a solid boundary can be decomposed into active and inactive components. Active turbulence consists of small-scale, high-frequency eddies that contribute directly and significantly to turbulent shear stress near the wall. In contrast, inactive turbulence originates from large-scale, low-frequency eddies characteristic of the outer region of the boundary layer. These eddies contribute to the turbulent kinetic energy near the ground but do not yield significant turbulent shear stress at the wall [22]. Observations show that large-scale eddies from the upper part of the ABL increase the TKE near the ground while having only a minor influence on the turbulent shear stress [23].

Two approaches have been used for the ABL modeling: a) the successor domain technique (SDT) and b) the precursor domain technique (PDT). The PDT enables the flow homogeneity due to the requirement for periodic boundary conditions at the inlet and outlet of the computational domain. This is not the case with the SDT, which uses defined flow profiles at the inlet and the Neumann boundary condition at the outlet, likely yielding a pressure gradient that causes alterations in the inlet profiles along the domain. When using the SDT, flow homogeneity should first be verified in an empty computational domain, and simulations involving buildings should only be performed once any inhomogeneity has been mitigated [10, 24].

In the SDT, inlet profiles are defined at the inlet surface of the computational domain, and the flow-driving forces are due to the imposed boundary conditions. In contrast, the PDT account for one or more forces that drive the flow through the computational domain, where the profiles are due to the flow. Thus, regarding the forces that cause the ABL flow, distinctions can be made: a) shear-force-driven ABL flow, b) pressure-gradient-driven ABL flow, c) uniform body-force-driven ABL flow, and d) non-uniform body-force-driven ABL flow, Fig. 2.

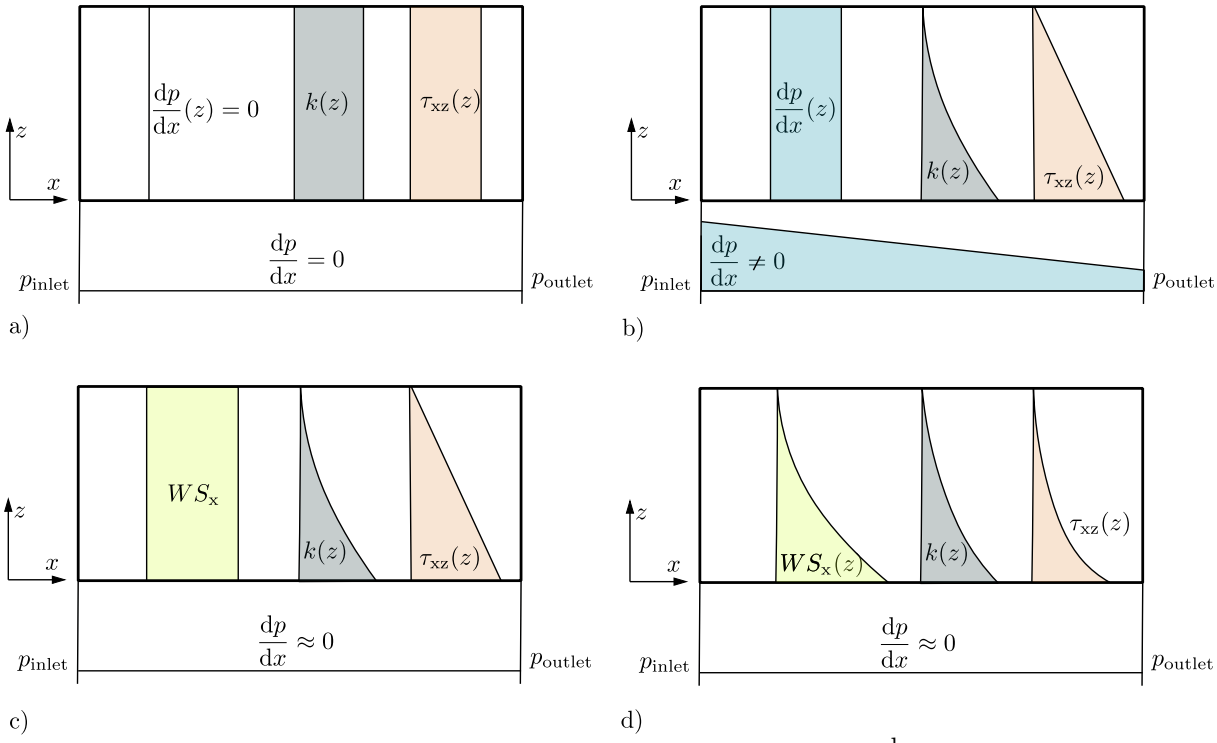

Figure 2. Schematic view of the distribution of pressure gradient $\frac{dp}{dx}$, TKE, and shear stress τ_{xz} for the studied ABL models: a) shear-stress driven (SSD, Section 2.2), b) pressure-driven (PD, Section 2.3), c) uniform body-force (BF, Section 2.4) driven, and d) non-uniform body-force driven.

It should be noted that both SDT and PDT rely on the same empty 2D domain: in the PDT this domain is used to generate homogeneous inlet profiles that are later mapped onto simulations with obstacles, whereas in the SDT the same empty domain is used only to verify that the prescribed inlet profiles do not create streamwise inhomogeneity. When the PDT is subsequently applied to a domain containing an obstacle, cyclic boundaries are no longer used; instead, the mapped inlet profiles are applied at the inlet and a Neumann boundary condition is imposed at the outlet, identical to the SDT setup.

The shear-stress-driven model was developed by deriving inlet profiles of the mean velocity, TKE, and TKE dissipation from the ABL equations. These profiles ensure horizontal flow homogeneity when using the standard $k-\varepsilon$ turbulence model together with the SDT [5]. This model, which yields the shear-stress-driven ABL flow, was complemented with the inlet profiles that enable the use of the RNG $k-\varepsilon$ and $k-\omega$ turbulence models, as well as the quasi-isotropic Reynolds stress transport turbulence model [16,25]. The correct shear stress boundary condition at the top surface of the computational domain must be applied to ensure horizontal flow homogeneity along the domain when using the SDT [26]. Otherwise, the inlet profiles change along the computational domain due to the effect of pressure gradient. This shear-stress-driven computational model is characterized by a constant distribution of the TKE and shear stress with increasing height [27], while atmospheric measurements show that such distributions may only occur in the lowest 10-15% of the ABL, i.e., the surface layer, not along the entire ABL height.

To mitigate this issue, the shear-stress-driven ABL model was enhanced by deriving inlet profiles of the TKE and TKE dissipation from the transport equation for the TKE. These inlet profiles are characterized by coefficients determined from laboratory or atmospheric measurements. These profiles, along with the application of the Neumann boundary condition at the top surface of the computational domain, ensure flow homogeneity using the standard $k-\epsilon$ turbulence model, where the TKE and shear stress decrease with increasing height. This model was further improved by defining inlet profiles that enable turbulence modeling using the $k-\omega$ SST turbulence model [27].

The constant shear-stress boundary condition at the top surface of the computational domain, [5], was modified to enable proper modeling of the shear-stress-driven ABL when using the SDT, [28], where the inlet profiles are generated using the PDT. It was shown that this boundary condition, together with predefined inlet profiles [5, 27], yields lower flow inhomogeneity error. The enhanced shear-stress-driven ABL model [27] was scrutinized [17, 18, 29–31] because the proposed inlet profiles only satisfy the

transport equation for the TKE, while they do not satisfy the momentum equation and the transport equation for the TKE dissipation. This issue was solved with the modification of the standard $k-\varepsilon$ turbulence model by using the turbulence model constants C_μ and σ_ε that vary along the height of the computational domain [29,32]. It was confirmed that this model can correctly simulate the flow separation and reattachment for the ABL flow over hilly terrains [33].

In the computational models outlined in [27,29,30,30,32–39], the flows are caused by a pressure gradient force or the concurrent application of the pressure gradient and shear forces. The first computational model of the ABL developed solely by the pressure gradient force (resulting from the pressure drop in the flow along the computational domain), [6], indicated the inlet profiles for the mean velocity, TKE, TKE dissipation, and specific TKE dissipation, based on the Deaves-Harris model for strong winds [40,41] and the ESDU 85020 [42] recommendations. These profiles ensure the proper simulation of the ABL using the standard $k-\varepsilon$, $k-\omega$, and $k-\omega$ SST turbulence models with the SDT. In this model, the results are consistent with the strong wind model, where the TKE and turbulent shear stress decrease linearly with increasing height.

The body-force-driven ABL model is developed by incorporating the force of a constant-magnitude in the momentum equation [43]. The magnitude of this force is determined based on the analysis of the forces governing the flow in the neutrally-stratified, steady, and homogeneous ABL, where the flow direction varies with height (wind veering). For the modeling purposes, the standard $k-\varepsilon$ turbulence model and the SDT were employed, yielding the TKE and shear stress profiles that vary with height. This approach was further extended to account for a variable distribution of this body force [44,45]. The body-force profile is obtained either from a known theoretical or experimental shear stress distribution by adjusting the distribution of the body force.

The paper is organized as follows. Section 2 presents the governing equations, the wall-function formulations, and the descriptions of the shear-stress-driven, pressure-driven, and body-force-driven unidirectional ABL models. Section 3 introduces two numerical examples: flow in an empty domain and flow over a cube. Section 4 provides the conclusions, while the appendix summarizes the ABL modeling approaches available in OpenFOAM-v2406 and includes detailed descriptions of the boundary conditions used.

2. Atmospheric Boundary Layer Models

The governing equations of the ABL are provided for isothermal, incompressible, single-phase flow with a neglected mass (gravitational) force. After applying Reynolds averaging technique, the continuity equation is given by

$$\frac{\partial \overline{u}_j}{\partial x_j} = 0, \tag{1}$$

and the momentum equation is given by

$$\frac{\partial \overline{u}_i}{\partial t} + \frac{\partial \overline{u}_i\,\overline{u}_j}{\partial x_j} - \frac{\partial}{\partial x_j}\left[\nu\left(\frac{\partial \overline{u}_i}{\partial x_j}\right)\right] = WS_i - \frac{1}{\rho}\frac{\partial \overline{p}}{\partial x_i} - \frac{\partial \overline{u_i' u_j'}}{\partial x_j}, \tag{2}$$

where $\overline{u_i}$ is the averaged velocity, $\bar{p}$ is the averaged pressure, $\overline{u_i' u_j'}$ is the Reynolds stress tensor, ν is the kinematic viscosity and WS_i is the (wind) source term, if applicable. Engineering ABL flows are characterised by high Reynolds numbers, for which molecular viscous stresses are negligible compared to Reynolds stresses. By neglecting molecular viscous stresses and introducing the assumptions of stationary, horizontally homogeneous, and unidirectional flow, the momentum equation reduces to

$$\frac{\partial}{\partial z}\left(\overline{u_x' u_z'}(z)\right) + \frac{1}{\rho}\frac{\partial \overline{p}}{\partial x} = WS_x(z). \tag{3}$$

Here, unidirectional flow implies that the velocity vector has only one non-zero component, $u_i = (u_x(z),\, 0,\, 0)$, while horizontal homogeneity ensures that all mean flow and turbulence quantities depend only on the vertical coordinate z. The only component of the Reynolds stress tensor is modelled using the Boussinesq approximation [46], yielding

$$-\frac{\partial}{\partial z}\,\nu_t\left(\frac{\partial \bar{u}_x}{\partial z}\right) + \frac{1}{\rho}\frac{\partial \bar{p}}{\partial x} = WS_x(z), \tag{4}$$

where ν_t is the turbulent viscosity, modelled using a two-equation turbulence model, e.g., $k-\varepsilon$, RNG $k-\varepsilon$, $k-\omega$, $k-\omega$ SST turbulence models.

In the remainder of this work, averaged physical quantities are used without the overbar notation. Additionally, u represents the x-component of the velocity vector u_x. All dimensional variables in this paper are expressed in SI units.

2.1. **Near-Wall Modelling.** In the ABL modeling, the near-ground region is not fully resolved; instead, wall functions are used to represent the flow characteristics close to the surface. Two types of wall functions are commonly employed for this purpose:

- a wall function based on the aerodynamic roughness length z_0 [5, 26],
- a wall function based on Nikuradse sand-grain roughness k_s [7, 12].

While roughness-based wall functions are essential for accurately representing the ABL over natural or urban terrain, many wind-engineering applications, such as wind loads on structures, strong-wind flow over impermeable surfaces, or pedestrian-level wind comfort studies, require modeling flow along smooth, impermeable walls. In such cases, a smooth-wall wall function is used, i.e., a formulation that does not include any roughness treatment [47].

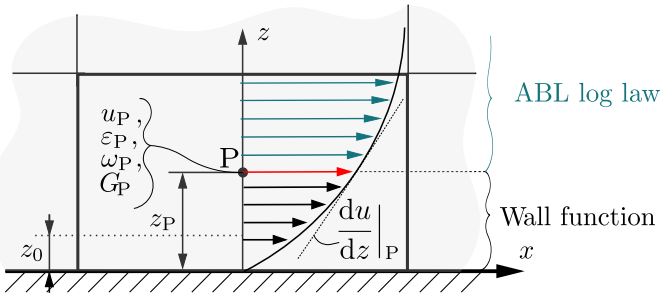

Figure 3. Schematic view of a wall adjacent control volume with its centroid at point P [7]. The wall function is used to calculate velocity u_P and turbulence parameters ω_P, ϵ_P.

2.1.1. *Rough wall function based on the aerodynamic surface roughness length z_0.* To ensure that the wall function correctly models the shear stress on the impermeable wall τ_w, the dissipation of the TKE at the centroid of the finite volume adjacent to the impermeable wall (point P) is given as [5, 26]

$$\varepsilon_P = \frac{u_\tau^3}{\kappa(z_P + z_0)}, \tag{5}$$

where z_P is the distance from the centroid of the finite volume to the impermeable wall, Fig. 3. When using a turbulence model based on the specific dissipation of the TKE (ω), the specific dissipation at point P is given by

$$\omega_P = \frac{u_\tau}{\kappa(z_P + z_0)}. \tag{6}$$

The friction velocity $u_\tau = \sqrt{\tau_w/\rho}$ can be determined from the TKE at point P, as

$$u_\tau = \sqrt[4]{C_\mu}\sqrt{k_P}, \tag{7}$$

while the production of TKE (G), which is used by the turbulence-model transport equations, is calculated at point P from the gradient of the mean velocity evaluated at P, as

$$G_P = \tau_w \left(\frac{du}{dz}\right)_P. \tag{8}$$

The shear stress on the impermeable wall can be determined as

$$\frac{\tau_w}{\rho} = \frac{u_P u_\tau \kappa}{\ln\left(\frac{z_P + z_0}{z_0}\right)}. \tag{9}$$

where u_P is the velocity at point P.

2.1.2. *Rough wall function based on the Nikuradse roughness k_s.* The wall function that accounts for surface roughness, based on the definition of Nikuradse roughness, was originally developed for solving flow problems in rough pipelines. In that original form, it is not suitable for the ABL simulations. To enable its application, it is necessary to determine an equivalent Nikuradse roughness length k_s based on the known aerodynamic surface roughness length z_0 [7].

The logarithmic law for the flow near an impermeable wall is modified to account for the surface roughness effects, as

$$u^+ = \frac{1}{\kappa}\left(\ln(E\,y^+)\right) - \Delta B = \frac{1}{\kappa}\left(\ln(E\,y^+) - \kappa\Delta B\right) = \frac{1}{\kappa}\ln\left(\frac{E\,y^+}{e^{\kappa\Delta B}}\right) = \frac{1}{\kappa}\ln\left(E^{`}y^+\right), \tag{10}$$

where $E^{`} = E/e^{\kappa\Delta B}$, $u^+ = u/u_\tau$ is the dimensionless velocity, $y^+ = zu_\tau/\nu$ is the dimensionless wall distance, E is the empirical constant and ΔB is the surface roughness function based on the dimensionless surface roughness $k_\mathrm{s}^+ = k_\mathrm{s}u_\tau/\nu$. By multiplying the left-hand side of Eqn. 10 by $u_\tau^2/(\tau_\mathrm{w}/\rho)$, where $u_\tau^2 = \tau_\mathrm{w}/\rho$, the shear stress on the wall is given by

$$\frac{\tau_\mathrm{w}}{\rho} = \frac{u_\mathrm{P}u_\tau}{\dfrac{1}{\kappa}\ln(E^{`}y^+)}. \tag{11}$$

Assuming a linear change in the velocity in the cell adjacent to the wall, the shear stress on the wall is given by

$$\frac{\tau_\mathrm{w}}{\rho} = \nu\frac{\mathrm{d}u}{\mathrm{d}z} = \nu_\mathrm{w}\left(\frac{u_\mathrm{P}-0}{z_\mathrm{P}}\right) = \nu_\mathrm{w}\frac{u_\mathrm{P}}{z_\mathrm{P}}, \tag{12}$$

which together, with Eqn. 11, yields the kinematic viscosity near the wall as

$$\nu_\mathrm{w} = \frac{z_\mathrm{P}u_\tau}{\dfrac{1}{\kappa}\ln(E^{`}y^+)}. \tag{13}$$

From the calculated value of the kinematic viscosity ν_w, it is possible to determine the turbulent viscosity ν_T near the wall, assuming $\nu_\mathrm{w} = \nu + \nu_\mathrm{T}$ and $\nu_\mathrm{T} = 0$ for $y^+ < 11.25$, where $y^+ = 11.25$ is the point obtained by equating the viscous-sublayer relation $u^+ = y^+$ with the logarithmic law $u^+ = (1/\kappa)\ln(Ey^+)$. The dissipation and specific dissipation of the TKE at point P are given as

$$\varepsilon_\mathrm{P} = \frac{u_\tau^3}{\kappa z_\mathrm{P}}, \tag{14}$$

$$\omega_\mathrm{P} = \frac{u_\tau}{\kappa z_\mathrm{P}}, \tag{15}$$

where the production of the TKE at point P is determined using Eqn. 8. For the general theoretical formulation of the wall function that accounts for the surface roughness using the Nikuradse surface roughness length [12], the relationship between the surface roughness and the aerodynamic height is given by $k_\mathrm{s} = 30z_0$. However, CFD implementations introduce an empirical mapping between k_s and z_0 to ensure consistency between wall functions and inlet velocity profiles [7]. In OpenFOAM, this mapping is obtained by matching the fully rough log-law wall function (`nutkRoughWallFunction`) with the Richards and Hoxey inlet profile (Eqn. 16), which yields $k_\mathrm{s} = 19.58z_0$ [48,49].

2.2. **Shear stress-driven unidirectional ABL.** The first ABL model, where the flow is driven by a prescribed shear stress on the top surface of the computational domain, was proposed by Richards and Hoxey [5]. This model was developed by deriving inlet profiles for the mean velocity $u(z)$, TKE $k(z)$, and TKE dissipation rate $\varepsilon(z)$ from the momentum equation and the transport equations for the TKE and its dissipation, given in the standard $k-\varepsilon$ turbulence model [5], as

$$u(z) = \frac{u_\tau}{\kappa}\ln\left(\frac{z+z_0}{z_0}\right), \tag{16}$$

$$k(z) = \frac{u_\tau^2}{\sqrt{C_\mu}} = \text{const.}, \tag{17}$$

$$\varepsilon(z) = \frac{u_\tau^3}{\kappa(z+z_0)}, \tag{18}$$

where $C_\mu = 0.09$ is the constant of the $k-\varepsilon$ turbulence model [5, 26]. The inlet profiles in Eqns. 16, 17 and 18 ensure flow homogeneity in the ABL simulation performed using the standard $k-\varepsilon$ turbulence model. It is essential to modify the turbulence model constant σ_ε according to

$$\sigma_\varepsilon = \frac{\kappa^2}{(C_2 - C_1)\sqrt{C_\mu}}, \tag{19}$$

which ensures the consistency of the momentum equation with the turbulence model equations. In Richards and Hoxey work [5], the proposed von Kármán constant is $\kappa = 0.4327$, while the turbulence model constants are $C_2 = 1.92$ and $C_1 = 1.44$. Consequently, from Eqn. 19 it follows that $\sigma_\varepsilon = 1.3$. Richards and Norris showed that the shear-driven ABL can also be modelled using the RNG $k-\varepsilon$ and $k-\omega$ turbulence models [16]. When applying the RNG $k-\varepsilon$ model, the inlet profiles follow Eqns. 16, 17, and 18. The only difference is that the constant C_μ is replaced by the value specified in the RNG model. If the Wilcox $k-\omega$ turbulence model is used, the inlet profiles for the mean velocity and TKE are defined using Eqns. 16 and 17. The profile for the specific dissipation rate of TKE must be prescribed at the inlet of the computational domain using the expression

$$\omega(z) = \frac{u_\tau}{\sqrt{\beta^*}\kappa(z + z_0)}, \tag{20}$$

where $\beta^* = 0.09$ is a constant of the $k-\omega$ turbulence model. When modeling a shear stress-driven ABL, it is essential to accurately define the stress on the top surface of the computational domain to ensure flow homogeneity [16–18]. Otherwise, errors in flow homogeneity may arise along the computational domain, yielding modifications of the inlet profiles and pressure gradient as an additional force influencing the flow. Table 1 outlines the boundary conditions, in accordance with Fig. 4. In the SDT, the inlet profiles are prescribed according to Eqns. 16, 17, 18 and 20. Meanwhile, in the PDT, both the inlet and outlet patches must either have periodic boundary conditions or a zero-gradient condition. In practice, a zero-gradient condition may be used since no streamwise gradients exist, but periodic boundary conditions are generally preferred because they provide significantly faster convergence.

This SSD approach to the ABL modeling yields the appropriate turbulent viscosity and stress, ensuring pressure-gradient-free flow along the computational domain. The calculated distributions of stress and TKE remain constant and do not change with increasing height, Fig. 4. These flow characteristics correspond to those of the ABL, i.e., the lowest portion of the ABL (typically the lowest 10% of its depth), often referred to as the inner surface layer [50, 51].

Table 1. Boundary conditions for the SSD ABL in the case of the SDT and PDT

	Inlet	Outlet	Top	Ground
SDT	`fixedValue`, profiles defined with Eqns. 16,17,20 and 18	`zeroGradient`	`uniform fixedValue` for turbulence quantities and velocity with SDT as the exception, where velocity uses `fixedShearStress`	Wall function based on aerodynamic roughness length or Nikuradse roughness (see Section 2.1).
PDT	`zeroGradient` or `cyclic`			

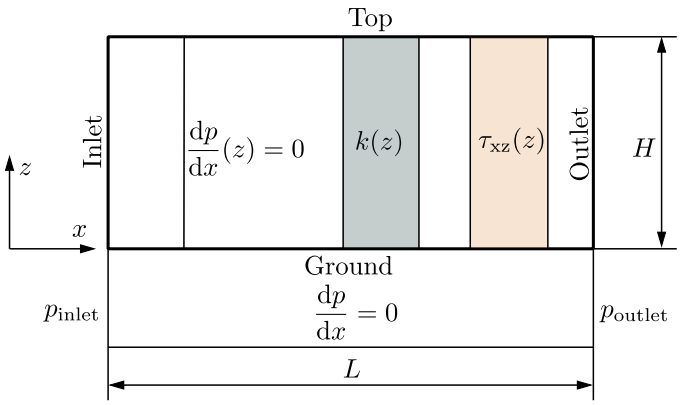

Figure 4. Schematic view of the distribution of the pressure gradient $\frac{\mathrm{d}p}{\mathrm{d}x}$, TKE, and shear stress τ_{xz} for the shear-stress-driven ABL.

2.3. **Pressure-driven unidirectional ABL.** The SSD ABL model exhibits limitations in accurately reproducing the decrease of TKE and shear-stress profiles with height, a feature characteristic of the lower atmosphere [50–52]. For this reason, the velocity profile in Eqn. 16 is used together with the modified inlet profiles for the TKE and its dissipation [27], given by

$$k(z) = \frac{u_\tau^2}{\sqrt{C_\mu}} \sqrt{B_1 \ln\left(\frac{z+z_0}{z_0}\right) + B_2}, \tag{21}$$

$$\varepsilon(z) = \frac{u_\tau^3}{\kappa(z+z_0)} \sqrt{B_1 \ln\left(\frac{z+z_0}{z_0}\right) + B_2}, \tag{22}$$

where B_1 and B_2 are constants defined from experiments using least square fit. It was confirmed that the SSD ABL can be generated by setting the parameters $B_1 = 0$ and $B_2 = 1$ [27]. The extension of the model to include TKE dissipation rate is given by Yang et al. [34], enabling the use of the $k-\omega$ SST turbulence model. The main drawback of this approach is that the proposed input profiles of Eqns. 16, 21 and 22 do not satisfy the momentum equation and the transport equation for the TKE dissipation [27,34]. Another disadvantage is the necessity of using the least squares method to define constants B_1 and B_2 in Eqns. 21 and 22.

A model has been developed to mitigate these shortcomings [6]. Its main advantage is that it is based on the Deaves–Harris formulation for strong-wind conditions [40], i.e., situations in which forced convection dominates and thermal stratification effects can be neglected. In this model, the mean velocity, TKE, and shear-stress profiles decrease with height. The input profiles for the mean velocity and turbulence at the inlet of the computational domain are given by

$$u(z) = \frac{u_\tau}{\kappa}\left(\ln\left(\frac{z}{z_0}\right) + C_{\mathrm{U1}}\left(\frac{z}{H}\right) + C_{\mathrm{U2}}\left(\frac{z}{H}\right)^2 + C_{\mathrm{U3}}\left(\frac{z}{H}\right)^3 + C_{\mathrm{U4}}\left(\frac{z}{H}\right)^4\right), \tag{23}$$

$$k(z) = u_\tau^2\left(C_{\mathrm{k1}} + C_{\mathrm{k2}}\left(1-\frac{z}{H}\right)^2 + C_{\mathrm{k3}}\left(1-\frac{z}{H}\right)^4 + C_{\mathrm{k4}}\left(1-\frac{z}{H}\right)^6\right), \tag{24}$$

$$\varepsilon(z) = \frac{C_\mu k(z)^2}{\kappa u_\tau z}\left(\begin{array}{l} 1 + (1+C_{\mathrm{U1}})\left(\frac{z}{H}\right) + (1 + C_{\mathrm{U1}} + 2\,C_{\mathrm{U2}})\left(\frac{z}{H}\right)^2 \\ + (1 + C_{\mathrm{U1}} + 2\,C_{\mathrm{U2}} + 3\,C_{\mathrm{U3}})\left(\frac{z}{H}\right)^3 \end{array}\right), \tag{25}$$

$$\omega(z) = \frac{k(z)}{\kappa u_\tau z}\left(\begin{array}{l} 1 + (1+C_{\mathrm{U1}})\left(\frac{z}{H}\right) + (1 + C_{\mathrm{U1}} + 2\,C_{\mathrm{U2}})\left(\frac{z}{H}\right)^2 \\ + (1 + C_{\mathrm{U1}} + 2\,C_{\mathrm{U2}} + 3\,C_{\mathrm{U3}})\left(\frac{z}{H}\right)^3 \end{array}\right), \tag{26}$$

where H is the height of the computational domain, while the remaining constants are provided in Tab. 2 for each turbulence model separately. The coefficients in Tab. 2, calculated for $\kappa = 0.4$, were obtained by solving the momentum equation and the turbulence model equations expressed in a dimensionless form using the finite difference method [6].

Table 2. The magnitudes of coefficients in the polynomials of input profiles; Eqns. 23, 24, 26 and 25 [6].

	C_{U1}	C_{U2}	C_{U3}	C_{U4}	C_{k1}	C_{k2}	C_{k3}	C_{k4}
$k-\varepsilon$	0.921	3.533	–1.926	0.805	0.528	0.385	–1.09	0.243
$k-\omega$	0.81	4.046	–2.623	1.1	0.333	–0.666	0.465	–0.349
$k-\omega$ SST	1.056	2.814	–0.834	0.297	0.28	–0.331	–0.334	0.096

At $H \geq h_{\mathrm{ABL}}/2$, where the ABL thickness is determined by the geostrophic height h_{ABL} [51], the derivatives of the mean velocity $\frac{\mathrm{d}u}{\mathrm{d}z}$ and turbulence parameters $\frac{\mathrm{d}k}{\mathrm{d}z}$, $\frac{\mathrm{d}\omega}{\mathrm{d}z}$, $\frac{\mathrm{d}\varepsilon}{\mathrm{d}z}$ tend to vanish, allowing diffusion to be neglected and a zero gradient to be prescribed at the top of the computational domain [40]. However, if the computational domain height H is less than the $h_{\mathrm{ABL}}/2$, it is necessary to give a constant mean velocity and appropriate values for the diffusion of turbulence parameters $\frac{\nu_{\mathrm{T}}(z=H)}{\sigma_k}\frac{\mathrm{d}k}{\mathrm{d}z}$, $\frac{\nu_{\mathrm{T}}(z=H)}{\sigma_\varepsilon}\frac{\mathrm{d}\varepsilon}{\mathrm{d}z}$ and $\frac{\nu_{\mathrm{T}}(z=H)}{\sigma_\omega}\frac{\mathrm{d}\omega}{\mathrm{d}z}$. These gradient values can be determined by differentiating the inlet profiles of Eqns. 24, 26 and 25. In the case of the PDT, velocity and turbulence parameters have a zero gradient at the inlet and outlet surfaces, while the average pressure is prescribed based on the pressure difference that governs the flow [6], as

$$\frac{1}{\rho}\frac{\mathrm{d}p}{\mathrm{d}x} = \frac{1}{\rho}\frac{p_{\mathrm{inlet}} - p_{\mathrm{outlet}}}{L} = -\frac{2}{\rho}\frac{u_\tau^2}{h_{\mathrm{ABL}}}. \tag{27}$$

By prescribing $p_{\mathrm{outlet}} = 0$, the pressure value at the inlet, from Eqn. 27, is given by

$$p_{\mathrm{inlet}} = 2L\frac{u_\tau^2}{h_{\mathrm{ABL}}} > 0. \tag{28}$$

The PDT can also be modeled by prescribing the inlet and outlet surfaces as periodic. In this case, an additional pressure gradient force must be included in the momentum equation and calculated according to Eqn. 27. Table 3 summarizes the boundary conditions for both the SDT and PDT.

Table 3. Boundary conditions for the PD ABL in the case of the SDT and PDT

	Inlet	Outlet	Top	Ground
SDT	`fixedValue`, profiles defined with Eqns. 23,24,26 and 25	`zeroGradient`	for $H \geq h_{\mathrm{ABL}}/2$ `zeroGradient`	Wall function based on aerodynamic roughness length or Nikuradse roughness (see Section 2.1).
PDT	`zeroGradient` $p_{\mathrm{inlet}} > 0$ or `cyclic` with a constant pressure gradient defined by Eqn. 27 and incorporated into the momentum equation.	`zeroGradient` $p_{\mathrm{outlet}} = 0$ or `cyclic` with a constant pressure gradient defined by Eqn. 27 and incorporated into the momentum equation.	for $H < h_{\mathrm{ABL}}/2$ `uniform` `fixedValue` for velocity and `uniform` `fixedGradient` for turbulence quantities	Wall function based on aerodynamic roughness length or Nikuradse roughness (see Section 2.1).

Figure 5 schematically illustrates the ABL simulation in which the flow is driven by a pressure gradient. The profiles of shear stress and TKE decrease approximately linearly with height. This model enables accurate numerical simulation of the lower portion of the ABL, from $z = 0$ to $z = h_{\mathrm{ABL}}/2$, where the flow is planar for strong-wind conditions. Above this height, rotational (Coriolis) effects become significant and the assumption of one-dimensional flow is no longer valid [51].

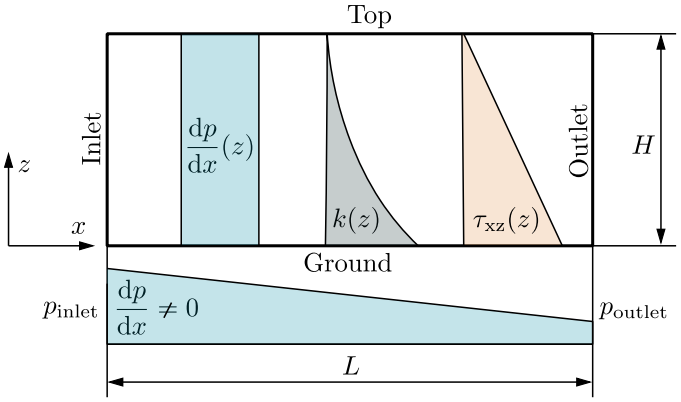

Figure 5. Schematic view of the distribution of pressure gradient $\frac{\mathrm{d}p}{\mathrm{d}x}$, TKE, and shear stress τ_{xz} for the pressure driven ABL.

2.4. **Body force driven unidirectional ABL.** The first ABL model with the flow driven by an additional body force [43] was developed without modifications to the turbulence model equations or boundary condition profiles. This was achieved by introducing a constant body force WS_x into the momentum equation (Eqn. 3), following LES evidence that the kinematic stress varies approximately linearly with height [53, 54]. The resulting expression is

$$\frac{\tau_{\mathrm{zx}}}{\rho} = -\overline{u'w'} = u_\tau^2 \left(1 - \frac{z}{h_{\mathrm{ABL}}}\right), \tag{29}$$

where the additional body force WS_{x} was derived from the fact that the divergence of stress in a neutrally temperature-stratified, stationary, and homogeneous ABL represents the drag force opposing the flow. To maintain the balance of forces in the ABL, the pressure gradient force and the Coriolis force must counteract the drag force, i.e., the divergence of stress. The known drag force allows for the determination of the driving force WS_{x}. This additional body force WS_{x} is thus calculated by differentiating the stress profile, with its constant magnitude due to the assumption of a linear stress distribution in Eqn. 29, as

$$WS_{\mathrm{x}} = \frac{1}{\rho}\frac{\mathrm{d}\tau_{\mathrm{zx}}}{\mathrm{d}z} = -\frac{u_\tau^2}{h_{\mathrm{ABL}}} = \mathrm{const.} \tag{30}$$

In Cindori et al. [44] and Cindori et al. [45], a model is proposed with the flow driven by the body force varying with the height. The distribution of this body force is obtained from Eqn. 4 by differentiating either the experimental or theoretical profile τ_{zx}^t, as

$$WS_{\mathrm{x}}(z) = \frac{1}{\rho}\frac{\mathrm{d}\tau_{\mathrm{zx}}^t(z)}{\mathrm{d}z}. \tag{31}$$

When using experimental stress distribution, it must be approximated or interpolated using a higher-order polynomial, typically of second or third degree. Since the experimental stress distribution is often unknown, the stress distribution in the ABL can be modeled using the Deaves-Harris model for strong winds [40]. To ensure that the body force distribution yields the intended shear stress distribution, it is necessary to adjust the body force distribution during convergence, as

$$WS_{\mathrm{x}}(z) = WS_{\mathrm{x}}(z)^* \frac{\tau_{\mathrm{zx}}^t(z)}{\tau_{\mathrm{zx}}^*(z)}, \tag{32}$$

where $\tau_{\mathrm{zx}}^*(z)$ and $WS_{\mathrm{x}}^*(z)$ are the body force and shear stress distribution from the previous iteration, respectively.

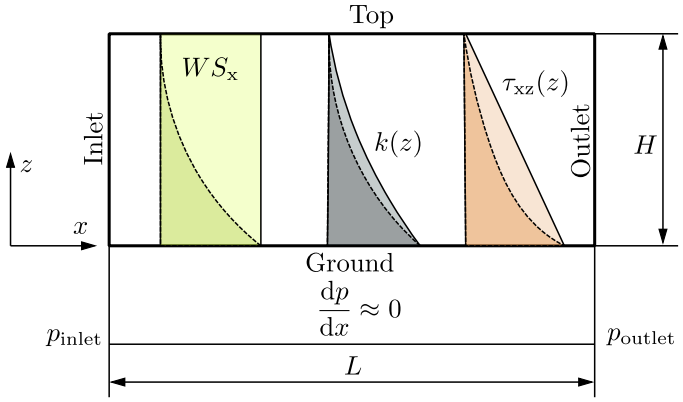

Figure 6. Schematic view of the distribution of pressure gradient $\frac{dp}{dx}$, TKE, and shear stress τ_{xz} for body-force driven ABL. The dashed line represents the case when body force changes with height z.

For body-force-driven ABL, the SDT can only be used after a PDT simulation, because unlike the PD or SSD approaches, no analytical expressions for inlet profiles exist. The SDT therefore relies entirely on the profiles obtained from the PDT run. When considering a variable body force, in addition to the stress distribution derived from experimental or theoretical results, it is crucial to determine the velocity and TKE profiles. This is because the velocity gradient is prescribed at the top surface, coupled with the value of the TKE, Tab. 4. TKE dissipation rate and specific TKE dissipation rate are calculated based on the TKE [44], as

$$\varepsilon(z=H) = C_\mu \frac{k(z=H)^2}{\nu_T(z=H)}, \quad \omega(z=H) = \frac{\varepsilon(z=H)}{\beta^* k(z=H)}. \tag{33}$$

For a constant body force, Cai et al. [43] proposed a computational domain height greater than the ABL height. In this approach, the body force is applied only in the ABL height, while the top boundary of the computational domain is set to the geostrophic wind speed with zero turbulence. As shown in Fig. 6, when the flow is driven by a constant body force, the stress varies linearly, similar to the pressure-driven ABL. Since the body force-driven ABL is not characterized by a pressure gradient, the applied body force effectively replaces its role. By varying the body force, a nonlinear distribution of the shear stress and TKE can be achieved while maintaining zero pressure gradient [49]. Accordingly, this ensures better agreement with the experimental and theoretical data.

Table 4. Boundary conditions for variable BF ABL in the case of the SDT and PDT

	Inlet	Outlet	Top	Ground
SDT	Input profiles generated using the PDT	`zeroGradient`	`uniform` `fixedGradient` for velocity and `uniform` `fixedValue` for turbulence quantities	Wall function based on aerodynamic roughness length or Nikuradse roughness (see Section 2.1).
PDT	`zeroGradient` or `cyclic`			

3. Numerical example, results and case set-up

The example for demonstration is widely utilized in previous relevant studies. [18] reported that this case can be traced back to the Computational Wind Engineering Conference 2000 competition [55] and it is based on the Silsoe full-scale testing site in the UK. Ever since, it has been used by many authors [6, 16, 26, 56]. The computational domain consists of a 500 m high and 5000 m long area, with a ground roughness of 10 mm. Computational domain consists of a 500 × 50 mesh with 1 cell in the y-direction to accommodate a two-dimensional calculation, see Fig. 7. Since the flow is homogeneous and unidirectional, the empty domain may also be three-dimensional, which does not affect the resulting profiles but only increases the computational cost.

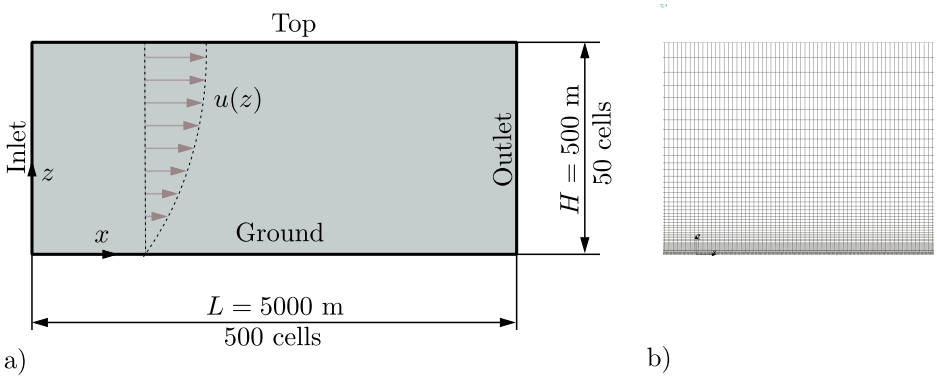

Figure 7. a) Schematic view of the 2D computational domain [6] and b) computational mesh (only a portion is displayed).

The inlet flow was characterized by a reference velocity of $u_{\text{ref}} = 10$ m/s at the reference height of $z_{\text{ref}} = 6$ m, with the aerodynamic surface roughness length of $z_0 = 0.01$ m, Table 5. The same case is available in the OpenFOAM tutorial directory under `tutorials/verificationAndValidation/atmosphericModels/atmDownstreamDevelopment`, where it is solved in a 3D setting, as described in Hargreaves and Wright work [26], using 50 cells in the y-direction.

Table 5. ABL characteristics [26], [6].

z_0 (m)	z_{ref} (m)	d (m)	u_{ref} (m/s)	κ (-)	u_τ (m/s)	h_{ABL} (m)
0.01	6	0	10	0.4	0.6252	1000

The simulations were conducted using the standard $k-\varepsilon$ turbulence model. Any RANS turbulence model could be used in this example; the $k-\varepsilon$ model was selected simply as a representative and widely adopted closure to illustrate the setup procedure. The choice is not essential for the demonstration. The boundary conditions for all types of ABLs are provided in Appendix A.2. Figures 8, 9, and 10 present the mean velocity and TKE profiles computed with OpenFOAM, alongside the available reference data for comparison. In all diagrams, OpenFOAM profiles are extracted from the cell centers of the first and last row of cells. In all cases, the variation of profiles is negligible, indicating that the flow can be considered homogeneous. For the body force-driven case, the body force was applied along the domain, with a zero-gradient condition prescribed for turbulent parameters and by prescribing the velocity from the logarithmic profile.

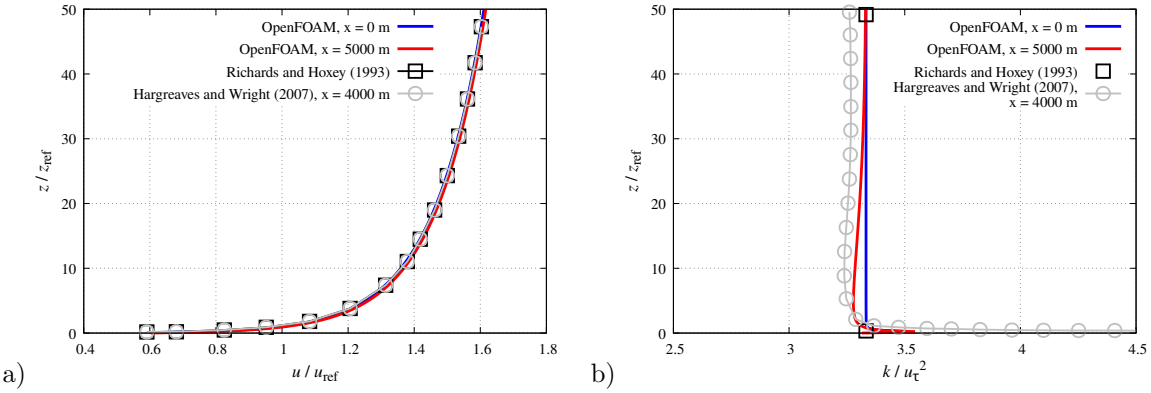

Figure 8. SSD ABL (SDT): a) velocity profile and b) TKE profile.

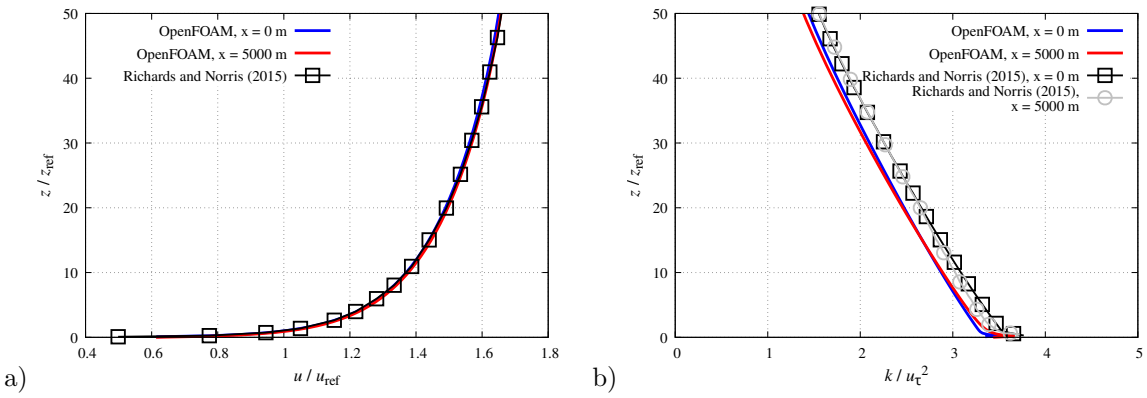

Figure 9. PD ABL (SDT): a) velocity profile and b) TKE profile.

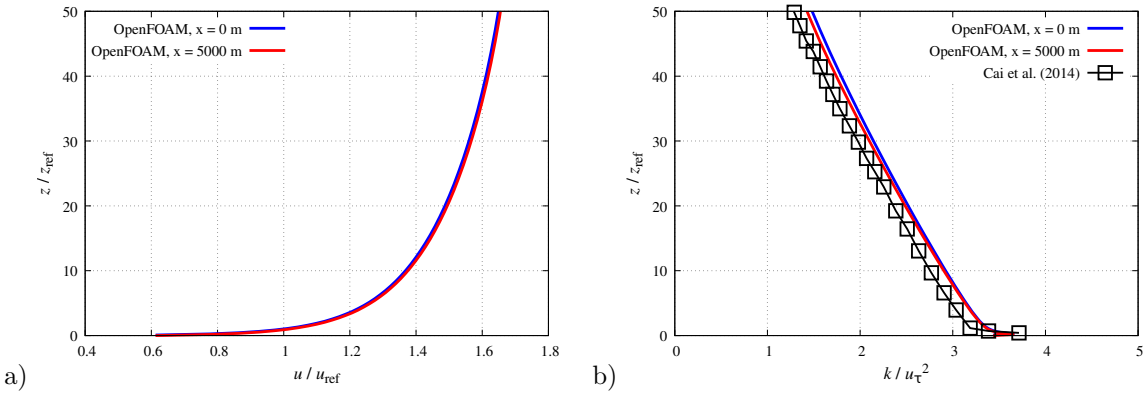

Figure 10. Uniform BF ABL (PDT): a) velocity profile and b) TKE profile.

A comparison between the SDT results and those obtained using the PDT is shown in Fig. 11. While the profiles do not match exactly due to differences in the methods used, the discrepancies are small enough that they are unlikely to affect the results when applied to actual cases.

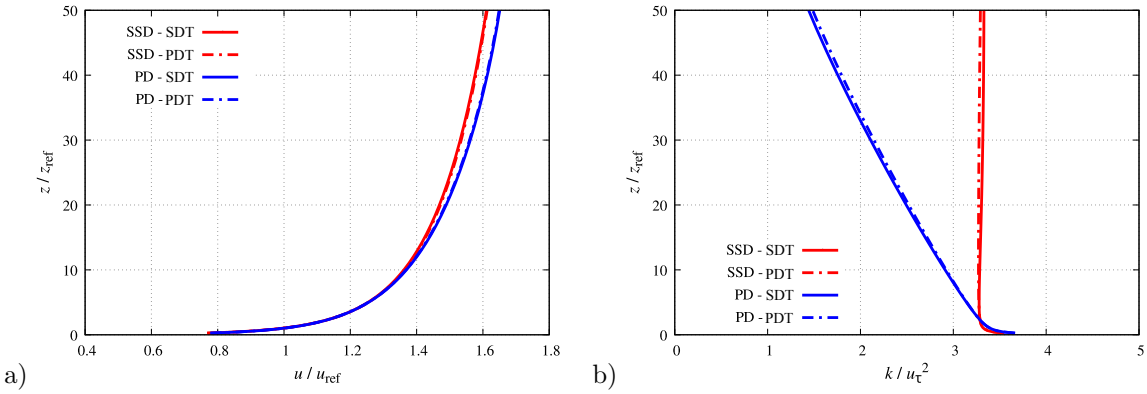

Figure 11. Comparison between SDT and PDT results in the case of PD and SSD ABL (at $x = 5000$ m): a) velocity profile and b) TKE profile.

4. **ABL modelling approach**

Given the variety of techniques for ABL modelling, selecting an ABL modelling approach can be challenging, especially for those not familiar with the literature [18]. This section provides a set of guidelines and a checklist to help decide on an ABL modelling technique and set up simulations effectively. These recommendations highlight key considerations in setting up a horizontally homogeneous ABL.
Key Considerations:

- SDT is generally more convenient to use, as it can be applied directly to the simulation of interest. However, regardless of the selected technique, it is essential to first perform an empty-domain simulation to verify flow homogeneity, i.e., to ensure that the inflow profiles remain in equilibrium with the domain. In some cases, running PDT is unavoidable. For example, in PD-ABL the formulation constants (see Table 2) assume a von Kármán constant of $\kappa = 0.4$. If a different κ is required, a precursor simulation must be carried out to generate consistent, self-equilibrated inflow profiles. Similarly, both uniform and non-uniform BF ABL methods require PDT, as analytical expressions for the corresponding inflow profiles are not available.
- The neutral ABL can be modelled with all common two-equation RANS turbulence models with similar accuracy. In practice, Menter's k–ω SST model often performs best, particularly in applications involving buildings and pedestrian wind studies, due to its superior treatment of near-wall behaviour and separation [57].
- There are multiple ways to create a neutral ABL flow in a simulation. A PD-ABL uses a uniform pressure gradient to sustain the flow, whereas a uniform BF-ABL applies a constant volumetric force throughout the domain to drive the flow. These two approaches are very similar, in a way that body force mimics pressure gradient. Non-uniform BF-ABL method go a step further by using a height-varying momentum source profile, which can be tuned so that the resulting equilibrium flow matches a desired velocity and shear-stress distribution exactly [44, 45]. This approach can be crucial if one needs to exactly reproduce the variation of shear with height, which might be important in high-accuracy dispersion simulations or when matching wind-tunnel profiles. However, the non-uniform body-force method is the most complex to set up, as it requires expressing the shear stress as a function of height. Nevertheless, this added complexity is worthwhile if one requires high accuracy in the vertical shear distribution.
- When deciding between an SSD-ABL model and a PD-ABL model, consider the vertical extent of the region of interest. In the lower portion of a neutral ABL (near the ground), the turbulent shear stress τ_{xz} is approximately constant with height (this is characteristic of the surface layer) [50]. Accordingly, for low-rise buildings or near-surface pedestrian wind studies, which involve only the lower part of the ABL, an SSD model is often adequate as it captures the constant near-surface shear stress well. On the other hand, for tall structures, a PD model is more appropriate to capture the linear shear-stress gradient through the ABL depth.
- In all cases, the use of wall functions specifically developed for ABL flows is a crucial requirement. These wall functions ensure consistency between the near-wall treatment and the imposed ABL profiles, particularly under rough-wall conditions, and their correct use is essential for maintaining horizontal homogeneity [5, 7, 26].
- Regardless of the ABL model used, standard wind engineering guidelines for computational domain dimensions should be followed when simulating objects in the ABL. Ensure that the domain is sufficiently large in the upstream, lateral, and vertical directions so that boundary effects do not interfere with the region of interest, see COST 732 [58] reconsiderations. In practice, one should keep the blockage ratio below recommended values (< 3 %) to minimise interference with domain boundaries [58, 59].

Below, we summarise the recommended SDT and PDT workflows for setting up ABL simulations:

- SDT approach: First, perform a simulation in an empty domain using the selected inlet velocity and turbulence profiles, ground roughness, and any driving force. Let the flow reach a steady state and confirm that the ABL profile remains horizontally homogeneous. Once the homogeneity is confirmed, the same inlet profiles and boundary condition settings are then applied in the domain containing the building or other object of interest, so that the inflow represents an already equilibrated ABL.
- PDT approach: Set up a simulation in an empty domain to develop the ABL flow. The precursor domain uses cyclic (periodic) boundary conditions at the streamwise inlet and outlet, allowing the flow to evolve toward a fully developed ABL that is internally consistent with the governing equations. As an efficient alternative to a finite 2D precursor domain, a 1D precursor simulation may also be used [28]. After the precursor simulation has converged, the resulting profiles are imposed as inlet conditions for the simulation of interest (the successor domain). Use zero-gradient conditions at the outlet, and a zero-gradient condition for pressure at the inlet, to allow the pressure field to adjust naturally. In effect, the main simulation now employs a numerically generated, dynamically consistent inflow rather than an analytic ABL profile. The precursor domain generates this inflow, and the successor domain uses it to simulate the scenario of interest.

Finally, Appendix A.1 summarises the ABL boundary conditions available in OpenFOAM-v2406 and relate them to the models discussed. While OpenFOAM-v2406 provides the inlet boundary condition for SSD-ABL, the PD-ABL boundary-condition implementations used in this work are included in the accompanying case files.

5. Conclusions

This study assesses steady RANS approaches to modeling the neutrally stratified ABL. Three major ABL modeling strategies, i.e., shear-stress-driven, pressure-driven, and body-force-driven, were analyzed based on theoretical formulation, implementation, and practical applications. The comparison highlights that each approach has its distinct features that require careful considerations. Several aspects are identified as critical for successful ABL simulations:

1) appropriate near-wall modeling [7, 24];
2) consistent and physically appropriate boundary conditions that match the selected ABL modeling strategy [18];
3) adherence to best-practice guidelines [58]; and
4) careful implementation in OpenFOAM, where flexibility in modifying models also increases the responsibility for ensuring numerical consistency.

The central contribution of this work is not only the systematic assessment of ABL modeling techniques, but also the emphasis on proper boundary-condition setup, which remains one of the most challenging and time-consuming steps for someone that is encountering ABL modeling for the first time. To support reproducibility and accelerate adoption, an accompanying public GitHub repository provides ready-to-use cases for the configurations discussed, and will be maintained and expanded by the authors. These cases are intended to serve as starting templates for more complex applications in wind engineering, such as structural aerodynamics, pedestrian-level wind comfort studies, or environmental flow simulations. By providing validated setups, the repository aims to reduce the need for users to construct cases from scratch or navigate the extensive and sometimes fragmented literature on this topic.

Acknowledgements

This work was supported by the Croatian Science Foundation under the project number HRZZ-IP-2022-10-9434. This paper has been funded by the European Union (NextGenerationEU) under the National Recovery and Resilience Plan 2021–2026 (NRRP), through the UNIZAG FSB institutional project "Structural aerodynamics", approved by the Ministry of Science, Education and Youth of the Republic of Croatia (component C3.2, source 581).

Author Contributions: Conceptualization, I.B. and M.C; methodology, I.B., M.C., and F.J.; software, I.B., M.C. and F.J.; validation, I.B.; formal analysis, I.B. and M.C; investigation, I.B. and M.C; resources, I.B. and M.C; data curation, I.B. and M.C; writing—original draft preparation, I.B., P.S., H.K.; writing—review and editing, I.B., M.C, P.S., S.K. and I.D.; visualization, I.B.; supervision, I.D., H.K. and S.K; project administration, H.K funding acquisition, H.K All authors have read and agreed to the published version of the manuscript.

Appendix A.

This appendix summarizes the available models, specifically the boundary conditions implemented in OpenFOAM, given the outlined theoretical framework. This may be useful for OpenFOAM users who are more familiar with its application.

A.1. **Available models in OpenFOAM®-v2406.** In `atmBoundaryLayer.C`, one can find inlet profiles for the velocity and turbulence parameters. These profiles are used by `atmBoundaryLayerInlet` collection of boundary conditions for inlet turbulence quantities and inlet velocity profile. The code to create the inlet velocity profile is provided in Lst. 1, which matches the velocity profile in Eqn. 16 with the addition of the displacement height d.

```
221     scalarField Un
222     (
223         (Ustar(z0)/kappa_)*log(((zDir() & pCf) - groundMin - d + z0)/z0)
224     );
```

Listing 1. Inlet velocity profile

The code for TKE is shown in Lst. 2, and the code for the TKE dissipation is shown in Lst. 3.

```
238     return
239         sqr(Ustar(z0))/sqrt(Cmu_)
240        *sqrt(C1_*log(((zDir() & pCf) - groundMin - d + z0)/z0) + C2_);
```

Listing 2. Turbulent kinetic energy

```
252     return
253         pow3(Ustar(z0))/(kappa_*((zDir() & pCf) - groundMin - d + z0))
254        *sqrt(C1_*log(((zDir() & pCf) - groundMin - d + z0)/z0) + C2_);
```

Listing 3. Turbulent kinetic energy dissipation rate

One can see that the equations for turbulence parameters are implemented following Eqns. 21 and 22 [27,34]. This is quite useful since, by setting $B_1 = 0$ and $B_2 = 1$ (those are default values), the equations for the shear-stress-driven ABL are maintained (Eqns. 17, 20 and 18). In the repository of this work, one can find the implementation of the pressure-driven ABL, as proposed by Richards and Norris [6], with the corresponding profiles of Eqns. 23, 24, 26 and 22.

For the near-wall modeling of the TKE dissipation rate, one can use the `atmEpsilonWallFunction` boundary condition, which employs Eqns. 5 and 7 for the cell value of the TKE dissipation rate [5] and is implemented as in Lst. 4.

```
221         scalar epsilonc =
222             w*Cmu75*pow(k[celli], 1.5)/(kappa*(y[facei] + z0[facei]));
```

Listing 4. Cell value of the TKE dissipation rate

This is coupled with the production of the TKE, computed at the first cell centroid as shown in Lst. 5.

```
221         scalar Gc =
222             w
223            *(nutw[facei] + nuw[facei])
224            *magGradUw[facei]
225            *Cmu25*sqrt(k[celli])
226            /(kappa*(y[facei] + z0[facei]));
```

Listing 5. The production term of the TKE

This approach is more preferred than integration over the first cell height, as it does not yield the peak of the TKE at the wall [30], which was observed by Richards and Hoxey [5] and Hargreaves and Wright [26]. The production of the TKE is calculated using Eqn. 8 with the velocity gradient at point P obtained by differencing Eqn. 16 and with wall shear stress calculated on the patch surface. The same equation for the production of the TKE is employed in the case of the specific TKE dissipation rate. The `atmOmegaWallFunction` uses Eqns. 6 and 7 for the cell value of the specific TKE dissipation rate, as shown in Lst. 6.

```
266     return Ustar(z0)/(kappa_*sqrt(Cmu_)*((zDir() & pCf) - groundMin - d + z0));
```

Listing 6. Cell value of the specific TKE dissipation rate

A.2. **ABL boundary conditions.** Tables 6-8 summarize the boundary conditions employed for shear stress, pressure-driven, and body-force-driven ABL results. For the shear-stress-driven and pressure-driven ABL, the boundary conditions are provided for the SDT, while boundary conditions for the PDT can be found in the GitHub repository and the manuscript case files.

Table 6. Boundary conditions for the SSD ABL in the case of the SDT. ω_P and ε_P are calculated using Eqns 5 and 6. Value of k, ε and ω at top and inlet are calculated using Eqns. 16, 17, 18 and 20. τ_{xz} is calculated from friction velocity $\tau_{xz} = \rho u_\tau^2$.

	Ground	Top	Inlet	Outlet
u	$u = 0$	τ_{xz} =const.	$u(z)$	$\frac{\mathrm{d}u}{\mathrm{d}n} = 0$
p	$\frac{\mathrm{d}p}{\mathrm{d}n} = 0$	$\frac{\mathrm{d}p}{\mathrm{d}n} = 0$	$\frac{\mathrm{d}p}{\mathrm{d}n} = 0$	$p = 0$
k	$\frac{\mathrm{d}k}{\mathrm{d}n} = 0$	k=const.	$k(z)$	$\frac{\mathrm{d}k}{\mathrm{d}n} = 0$
ε	$\varepsilon_P = \frac{u_\tau^3}{\kappa(z_0 + z_P)}$	ε=const.	$\varepsilon(z)$	$\frac{\mathrm{d}\varepsilon}{\mathrm{d}n} = 0$
ω	$\omega_P = \frac{u_\tau}{\kappa(z_P + z_0)}$	ω=const.	$\omega(z)$	$\frac{\mathrm{d}\omega}{\mathrm{d}n} = 0$

Table 7. Boundary conditions for the PD ABL in the case of the SDT and $H \geq h_{\mathrm{ABL}}/2$. ω_P and ε_P are calculated using Eqns 5 and 6. Value of k, ε and ω at top and inlet are calculated using Eqns. 23, 24, 25 and 26.

	Ground	Top	Inlet	Outlet
u	$u = 0$	u=const.	$u(z)$	$\frac{\mathrm{d}u}{\mathrm{d}n} = 0$
p	$\frac{\mathrm{d}p}{\mathrm{d}n} = 0$	$\frac{\mathrm{d}p}{\mathrm{d}n} = 0$	$\frac{\mathrm{d}p}{\mathrm{d}n} = 0$	$p = 0$
k	$\frac{\mathrm{d}k}{\mathrm{d}n} = 0$	$\frac{\mathrm{d}k}{\mathrm{d}n} = 0$	$k(z)$	$\frac{\mathrm{d}k}{\mathrm{d}n} = 0$
ε	$\varepsilon_P = \frac{u_\tau^3}{\kappa(z_0 + z_P)}$	$\frac{\mathrm{d}\varepsilon}{\mathrm{d}n} = 0$	$\varepsilon(z)$	$\frac{\mathrm{d}\varepsilon}{\mathrm{d}n} = 0$
ω	$\omega_P = \frac{u_\tau^3}{\kappa(z_0 + z_P)}$	$\frac{\mathrm{d}\omega}{\mathrm{d}n} = 0$	$\omega(z)$	$\frac{\mathrm{d}\omega}{\mathrm{d}n} = 0$

Table 8. Boundary conditions for the constant BF ABL in the case of the PDT. ω_P and ε_P are calculated using Eqns 5 and 6. Velocity at the top surface is calculated from logarithmic profile, i.e. Eqn. 16.

	Ground	Top	Inlet	Outlet
u	$u = 0$	u=const.	$\frac{\mathrm{d}u}{\mathrm{d}n} = 0$	$\frac{\mathrm{d}u}{\mathrm{d}n} = 0$
p	$\frac{\mathrm{d}p}{\mathrm{d}n} = 0$	$\frac{\mathrm{d}p}{\mathrm{d}n} = 0$	$\frac{\mathrm{d}p}{\mathrm{d}n} = 0$	$p = 0$
k	$\frac{\mathrm{d}k}{\mathrm{d}n} = 0$	$\frac{\mathrm{d}k}{\mathrm{d}n} = 0$	$\frac{\mathrm{d}k}{\mathrm{d}n} = 0$	$\frac{\mathrm{d}k}{\mathrm{d}n} = 0$
ε	$\varepsilon_P = \frac{u_\tau^3}{\kappa(z_0 + z_P)}$	$\frac{\mathrm{d}\varepsilon}{\mathrm{d}n} = 0$	$\frac{\mathrm{d}\varepsilon}{\mathrm{d}n} = 0$	$\frac{\mathrm{d}\varepsilon}{\mathrm{d}n} = 0$
ω	$\omega_P = \frac{u_\tau^3}{\kappa(z_0 + z_P)}$	$\frac{\mathrm{d}\omega}{\mathrm{d}n} = 0$	$\frac{\mathrm{d}\omega}{\mathrm{d}n} = 0$	$\frac{\mathrm{d}\omega}{\mathrm{d}n} = 0$

References

[1] H. Wurps, G. Steinfeld, and S. Heinz, "Grid-resolution requirements for large-eddy simulations of the atmospheric boundary layer," *Boundary-Layer Meteorology*, vol. 175, no. 2, pp. 179–201, 2020.

[2] M. Bervida, L. Patruno, S. Stanič, and S. de Miranda, "Synthetic generation of the atmospheric boundary layer for wind loading assessment using spectral methods," *Journal of Wind Engineering and Industrial Aerodynamics*, vol. 196, p. 104040, 2020.

[3] R. Vasaturo, I. Kalkman, B. Blocken, and P. Van Wesemael, "Large eddy simulation of the neutral atmospheric boundary layer: performance evaluation of three inflow methods for terrains with different roughness," *Journal of Wind Engineering and Industrial Aerodynamics*, vol. 173, pp. 241–261, 2018.
[4] D. Muñoz-Esparza and B. Kosović, "Generation of inflow turbulence in large-eddy simulations of nonneutral atmospheric boundary layers with the cell perturbation method," *Monthly Weather Review*, vol. 146, no. 6, pp. 1889–1909, 2018.
[5] P. Richards and R. Hoxey, "Appropriate boundary conditions for computational wind engineering models using the k-ε turbulence model," *Journal of Wind Engineering and Industrial Aerodynamics*, vol. 46, pp. 145–153, 1993.
[6] P. Richards and S. Norris, "Appropriate boundary conditions for a pressure driven boundary layer," *Journal of Wind Engineering and Industrial Aerodynamics*, vol. 142, pp. 43–52, 2015.
[7] B. Blocken, T. Stathopoulos, and J. Carmeliet, "Cfd simulation of the atmospheric boundary layer: wall function problems," *Atmospheric Environment*, vol. 41, no. 2, pp. 238–252, 2007.
[8] A. Townsend, "Equilibrium layers and wall turbulence," *Journal of Fluid Mechanics*, vol. 11, no. 1, pp. 97–120, 1961.
[9] ——, *The structure of turbulent shear flow*. Cambridge University Press, 1976.
[10] B. Blocken, J. Carmeliet, and T. Stathopoulos, "Cfd evaluation of wind speed conditions in passages between parallel buildings—effect of wall-function roughness modifications for the atmospheric boundary layer flow," *Journal of Wind Engineering and Industrial Aerodynamics*, vol. 95, no. 9-11, pp. 941–962, 2007.
[11] S. B. Pope, "Turbulent flows," *Measurement Science and Technology*, vol. 12, no. 11, pp. 2020–2021, 2001.
[12] T. Cebeci and P. Bradshaw, "Momentum transfer in boundary layers," *Washington*, 1977.
[13] H. A. Panofsky and J. A. Dutton, "Atmospheric turbulence. models and methods for engineering applications," *New York: Wiley*, 1984.
[14] P. Richards, R. Hoxey, B. Connell, and D. Lander, "Wind-tunnel modelling of the silsoe cube," *Journal of Wind Engineering and Industrial Aerodynamics*, vol. 95, no. 9-11, pp. 1384–1399, 2007.
[15] M. Bottema, "Turbulence closure model "constants" and the problems of "inactive" atmospheric turbulence," *Journal of Wind Engineering and Industrial Aerodynamics*, vol. 67, pp. 897–908, 1997.
[16] P. Richards and S. Norris, "Appropriate boundary conditions for computational wind engineering models revisited," *Journal of Wind Engineering and Industrial Aerodynamics*, vol. 99, no. 4, pp. 257–266, 2011.
[17] P. J. Richards and S. E. Norris, "Appropriate boundary conditions for computational wind engineering: Still an issue after 25 years," in *The 7th International Symposium on Computational Wind Engineering*, Seoul, South Korea, June 2018, 18–22 June 2018.
[18] ——, "Appropriate boundary conditions for computational wind engineering: Still an issue after 25 years," *Journal of Wind Engineering and Industrial Aerodynamics*, vol. 190, pp. 245–255, 2019.
[19] K. G. McNaughton and Y. Brunet, "Townsend's hypothesis, coherent structures and monin–obukhov similarity," *Boundary-Layer Meteorology*, vol. 102, pp. 161–175, 2002.
[20] J. F. Morrison, "The interaction between inner and outer regions of turbulent wall-bounded flow," *Philosophical Transactions of the Royal Society A: Mathematical, Physical and Engineering Sciences*, vol. 365, no. 1852, pp. 683–698, 2007.
[21] T. Mikkelsen, S. E. Larsen, H. E. Jørgensen, P. Astrup, and X. G. Larsén, "Scaling of turbulence spectra measured in strong shear flow near the earth's surface," *Physica Scripta*, vol. 92, no. 12, p. 124002, 2017.
[22] P. Davidson, *Turbulence: an introduction for scientists and engineers*. Oxford University Press, 2015.
[23] A. Grant, "The structure of turbulence in the near-neutral atmospheric boundary layer," *Journal of the Atmospheric Sciences*, vol. 49, no. 3, pp. 226–239, 1992.
[24] Y. Abu-Zidan, P. Mendis, and T. Gunawardena, "Impact of atmospheric boundary layer inhomogeneity in cfd simulations of tall buildings," *Heliyon*, vol. 6, no. 7, 2020.
[25] B. E. Launder, G. J. Reece, and W. Rodi, "Progress in the development of a reynolds-stress turbulence closure," *Journal of Fluid Mechanics*, vol. 68, no. 3, pp. 537–566, 1975.
[26] D. Hargreaves and N. Wright, "On the use of the k–ε model in commercial cfd software to model the neutral atmospheric boundary layer," *Journal of Wind Engineering and Industrial Aerodynamics*, vol. 95, no. 5, pp. 355–369, 2007. [Online]. Available: https://www.sciencedirect.com/science/article/pii/S016761050600136X
[27] Y. Yang, M. Gu, S. Chen, and X. Jin, "New inflow boundary conditions for modelling the neutral equilibrium atmospheric boundary layer in computational wind engineering," *Journal of Wind Engineering and Industrial Aerodynamics*, vol. 97, no. 2, pp. 88–95, 2009.
[28] J. O'Sullivan, R. Archer, and R. Flay, "Consistent boundary conditions for flows within the atmospheric boundary layer," *Journal of Wind Engineering and Industrial Aerodynamics*, vol. 99, no. 1, pp. 65–77, 2011.
[29] C. Gorlé, J. van Beeck, and P. Rambaud, "Dispersion in the wake of a rectangular building: validation of two reynolds-averaged navier–stokes modelling approaches," *Boundary-Layer Meteorology*, vol. 137, pp. 115–133, 2010.
[30] A. Parente, C. Gorlé, J. Van Beeck, and C. Benocci, "Improved k–ε model and wall function formulation for the rans simulation of abl flows," *Journal of Wind Engineering and Industrial Aerodynamics*, vol. 99, no. 4, pp. 267–278, 2011.
[31] A. Parente, C. Gorlé, J. van Beeck, and C. Benocci, "A comprehensive modelling approach for the neutral atmospheric boundary layer: consistent inflow conditions, wall function and turbulence model," *Boundary-Layer Meteorology*, vol. 140, no. 3, pp. 411–428, 2011.
[32] C. v. Gorlé, J. Van Beeck, P. Rambaud, and G. Van Tendeloo, "Cfd modelling of small particle dispersion: the influence of the turbulence kinetic energy in the atmospheric boundary layer," *Atmospheric Environment*, vol. 43, no. 3, pp. 673–681, 2009.
[33] M. Balogh, A. Parente, and C. Benocci, "Rans simulation of abl flow over complex terrains applying an enhanced k-ε model and wall function formulation: Implementation and comparison for fluent and openfoam," *Journal of Wind Engineering and Industrial Aerodynamics*, vol. 104, pp. 360–368, 2012.
[34] Y. Yang, Z. Xie, and M. Gu, "Consistent inflow boundary conditions for modelling the neutral equilibrium atmospheric boundary layer for the SST k-ω model," *Wind and Structures*, vol. 24, no. 5, pp. 465–480, 2017.

[35] P. Hu, Y. Li, C. Cai, H. Liao, and G. Xu, "Numerical simulation of the neutral equilibrium atmospheric boundary layer using the sst k-ω turbulence model," *Wind and Structures*, vol. 17, no. 1, pp. 87–105, 2013.
[36] F. Juretić and H. Kozmar, "Computational modeling of the neutrally stratified atmospheric boundary layer flow using the standard k–ε turbulence model," *Journal of Wind Engineering and Industrial Aerodynamics*, vol. 115, pp. 112–120, 2013.
[37] M. Balogh and A. Parente, "Realistic boundary conditions for the simulation of atmospheric boundary layer flows using an improved k–ε model," *Journal of Wind Engineering and Industrial Aerodynamics*, vol. 144, pp. 183–190, 2015.
[38] B. Yan, Q. Li, Y. He, and P. Chan, "Rans simulation of neutral atmospheric boundary layer flows over complex terrain by proper imposition of boundary conditions and modification on the k-ε model," *Environmental Fluid Mechanics*, vol. 16, pp. 1–23, 2016.
[39] R. Longo, M. Ferrarotti, C. G. Sánchez, M. Derudi, and A. Parente, "Advanced turbulence models and boundary conditions for flows around different configurations of ground-mounted buildings," *Journal of Wind Engineering and Industrial Aerodynamics*, vol. 167, pp. 160–182, 2017.
[40] D. Deaves, "A mathematical model of the structure of strong winds," *CIRIA Report 76, Const. Ind. Research and Inf. Assoc.*, 1978.
[41] D. Deaves and R. Harris, "A note on the use of asymptotic similarity theory in neutral atmospheric boundary layers," *Atmospheric Environment*, vol. 16, no. 8, pp. 1889–1893, 1982.
[42] E. D. item 85020, "Characteristics of atmospheric turbulence near the ground, part ii: single point data for strong winds (neutral atmosphere)," *Engineering Science Data Unit.*, 1985.
[43] X. Cai, Q. Huo, L. Kang, and Y. Song, "Equilibrium atmospheric boundary-layer flow: computational fluid dynamics simulation with balanced forces," *Boundary-Layer Meteorology*, vol. 152, no. 3, pp. 349–366, 2014.
[44] M. Cindori, F. Juretić, H. Kozmar, and I. Džijan, "Steady rans model of the homogeneous atmospheric boundary layer," *Journal of Wind Engineering and Industrial Aerodynamics*, vol. 173, pp. 289–301, 2018.
[45] M. Cindori, I. Džijan, F. Juretić, and H. Kozmar, "The atmospheric boundary layer above generic hills: computational model of a unidirectional body force-driven flow," *Boundary-Layer Meteorology*, vol. 176, pp. 159–196, 2020.
[46] J. Boussinesq, *Essai sur la théorie des eaux courantes*. Impr. nationale, 1877.
[47] B. E. Launder and D. B. Spalding, "The numerical computation of turbulent flows," in *Numerical prediction of flow, heat transfer, turbulence and combustion*, 1983, pp. 96–116.
[48] B. Martinez, "Wind resource in complex terrain with openfoam," *Risø DTU, National Laboratory for Sustainable Energy*, 2011.
[49] M. Cindori, "Computational modeling of the body force-driven homogeneous atmospheric boundary layer," Ph.D. dissertation, University of Zagreb. Faculty of Mechanical Engineering and Naval Architecture, 2021.
[50] J. R. Garratt, *The atmospheric boundary layer*. Cambridge, UK: Cambridge University Press, 1992.
[51] R. B. Stull, *An introduction to boundary layer meteorology*, 1st ed. Dordrecht, Netherlands: Kluwer Academic Publishers, 1988, vol. 13.
[52] J. C. Wyngaard, *Turbulence in the Atmosphere*. Cambridge University Press, 2010.
[53] A. Andren, A. R. Brown, P. J. Mason, J. Graf, U. Schumann, C.-H. Moeng, and F. T. Nieuwstadt, "Large-eddy simulation of a neutrally stratified boundary layer: A comparison of four computer codes," *Quarterly Journal of the Royal Meteorological Society*, vol. 120, no. 520, pp. 1457–1484, 1994.
[54] F. Porté-Agel, C. Meneveau, and M. B. Parlange, "A scale-dependent dynamic model for large-eddy simulation: application to a neutral atmospheric boundary layer," *Journal of Fluid Mechanics*, vol. 415, pp. 261–284, 2000.
[55] P. Richards, A. Quinn, and S. Parker, "A 6 m cube in an atmospheric boundary layer flow-part 2. computational solutions," *Wind and Structures*, vol. 5, no. 2_3_4, pp. 177–192, 2002.
[56] D. S. Abdi and G. T. Bitsuamlak, "Wind flow simulations in idealized and real built environments with models of various level of complexity," *Wind and Structures*, vol. 22, no. 4, pp. 503–524, 2016.
[57] M. Cindori, P. Čajić, I. Džijan, F. Juretić, and H. Kozmar, "A comparison of major steady rans approaches to engineering abl simulations," *Journal of Wind Engineering and Industrial Aerodynamics*, vol. 221, p. 104867, 2022.
[58] J. Franke, A. Hellsten, K. H. Schlunzen, and B. Carissimo, "Best practice guideline for the cfd simulation of flows in the urban environment." *Cost action 732: quality assurance and improvement of microscale meteorological models.*, 2007.
[59] Y. Abu-Zidan, P. Mendis, and T. Gunawardena, "Optimising the computational domain size in cfd simulations of tall buildings," *Heliyon*, vol. 7, no. 4, 2021.